Enhancing PET/CT Assessment with Porous 3D-Printed Grids – A Pilot Study

Sai Kiran Kumar Nalla[1], Quentin Maronnier[3], John A. Kennedy[4,5], Tala Palchan-Hazan[4], Olivier Caselles[2,3 *]

1. Institut universitaire du cancer de Toulouse - IUTC, Université de Toulouse, 31400 Toulouse, France
2. Tachyons SAS, Toulouse, France
3. Department of Medical Physics, Institut Claudius Regaud, Toulouse, France
4. Department of Nuclear Medicine, Rambam Health Care Campus, P.O.B. 9602, 3109601 Haifa, Israel
5. Ruth and Bruce Rappaport Faculty of Medicine, Technion Israel Institute of Technology, Haifa, Israel

***Correspondance :** Olivier Caselles **(caselles.olivier@iuct-oncopole.fr)**

ORCID IDS :

Sai Kiran Kumar Nalla : 0000-0002-8044-6330

Quentin Marronnier : 0000-0002-2266-9122

John A Kennedy**:** 0000-0002-2043-4397

Tala Palchan-Hazan: 0009-0004-2632-1168

Olivier Caselles: 0000-0002-5404-5066

NOTE: This preprint reports new research that is not certified by peer review and should not be used to guide clinical practice.

Abstract:

Objective: Phantom experiments are widely used for standardisation in positron emission tomography (PET), but current practices to do not necessarily reflect clinical reality (e.g. targets have visible walls) and require meticulous phantom preparation for repeatability. Three-dimensional (3D) printing can reduce these limitations by optimizing preparatory methods and improving phantom features. This work proposes employing 3D-printed porous grids as an alternative to fillable targets, and characterizes the same.

Approach: Acrylonitrile butadiene styrene cubic grids (4 cm/side) with varying pore distance (5, 7, 10 mm) and solidity (50%, 60%, 70%) were printed. Spherical targets of 10, 15 and 20 mm were also incorporated for quantitation and detectability. Grids were immersed in a [^{18}F] fluorodeoxyglucose solution (activity: ~7 kBq/mL), with soap, within a Jaszczak phantom cylinder. Five consecutive acquisitions were repeated on five different days (Day 0,1,4-6) using a Discovery MI PET/CT (GE Healthcare). Hounsfield units (HU), recovery coefficient (RC) and dilution coefficient (DC) were the metrics used for analysis. A Friedman test was utilized to study global statistical significance across days, with Wilcoxon tests for pairwise differences between days.

Main Results: Within the grids, HU values (range −40 to −21, Day 0) increased with time (range −28 to −4, Day 6). The 5 mm pore distance grid provided features with the best resolution. PET quantification showed consistent results across trials, confirming robustness. Achieved target-to-background ratios (mean±std. dev.) were 1.93±0.14, 2.44±0.2, and 3.01±0.08 vs. 2, 2.5 and 3.33 (theoretical), respectively. Observed RC were in range of 0.4 – 1.2. RC Correlation across days was strong ($p \geq 0.67$), and days 1 and 5 had the best pairwise comparable results.

Significance: 3D-printed grids offer a reliable, reproducible alternative for PET/CT assessment. Dozens of targets with background were produced with a single tracer administration. CT attenuation throughout the phantom mimicked water, giving good PET representation of wall-free targets.

Keywords: Additive manufacturing, Fused deposition modeling, Quantitative PET/CT, Nuclear medicine, Rapid prototyping, Radionuclide imaging

NOTE: This preprint reports new research that is not certified by peer review and should not be used to guide clinical practice.

1. Introduction:

Quality control (QC) in nuclear medicine (NM) is important for enabling accuracy, reliability, and safety of both diagnostic and therapeutic procedures, particularly in hybrid imaging modalities like positron emission tomography/x-ray computed tomography (PET/CT) and single photon emission computed tomography/CT (SPECT/CT) (1–3). A large variety of test objects (phantoms) are typically used (4). These include Jaszczak, NEMA (National Electrical Manufacturers Association), Hoffman brain, and IEC (International Electrotechnical Commission) body phantoms. Phantoms usually contain multiple compartments and inserts, such as acrylic spheres, to simulate lesions and surrounding tissue. By meticulously filling these compartments and inserts with various radiotracer activity concentrations, these phantoms support the assessment of lesion detection and quantitation (5–7). One of the notable limitations in the conventional protocols using acrylic spheres in QC is that variations in actual versus intended activity concentrations on PET, accompanied by the "wall effect" (artifactual contrast due to solid walls of the spheres), reduce the clinical relevance of such inserts (8–11). Moreover, the number of features and their mounting positions are fixed (12–14). Therefore, assessment is constrained to specific predetermined locations with limited customizability in the imaging field of view (FOV). Phantom preparation can be time consuming due to multi-compartment filling which increases the potential for preparation errors (7,15). Often this means higher radiation exposure for technicians and physicists performing such tests and further limits the practicality of frequent experiments (16).

While useful for standardization, phantom experiments fail to replicate the complex anatomical variability seen in clinical reality (2). This limitation becomes increasingly challenging as PET/CT spatial resolution improves significantly with each new generation of scanners. The need to be able to test smaller synthetic lesions (<1 cm) or lesion heterogeneity is increasing (7). Also, the lack of patient-dependent variability and realistic material properties within standard phantoms limits their usage

NOTE: This preprint reports new research that is not certified by peer review and should not be used to guide clinical practice.

(17,18) to assess AI (artificial intelligence) based algorithms. With its versatile potential, 3D printing has been reported previously to address these shortcomings and bridge the gaps between physicists and physicians (19–33). In the context of PET/CT applications, 3D printing has been used to create complex anatomical phantoms closer to clinic reality with customizable targets emulating lesions, thus complementing the features of modern scanning technology (25,34,35) . The two major cost-effective methods of 3D printing, namely fused deposition modelling (FDM) and stereolithography (SLA), have been widely utilized in research for the fabrication of phantoms. Studies using polyjet printing have also been reported for (25,27,33) but they come at considerably higher cost. From the perspective of synthetic lesion creation, spherical inserts similar to acrylic spheres were 3D-printed using both FDM, SLA (29). While this approach showed a reduction in the wall effect, it is not completely eliminated. A few studies provided some advancements in creating heterogeneous synthetic lesion inserts (35). By producing several small fillable compartments within segmented synthetic lesions, more intricate radiotracer uptake patterns can be represented. While this is a significant improvement in phantom design, filling of these multiple small compartments is a challenge in practice. In a few other studies, radioactive synthetic lesions were created via 3D printing by directly mixing radiotracer into the resin (19,26,27,32) and embedding printed inserts within phantoms. Though the findings are promising, this requires a shielded environment with specific ambient conditions for printing. Another limitation is its suitability only for long half-life tracers, or comparatively high activity concentrations for short half-life tracers accounting for time required for printing and acquisition. A more practical approach involves using 3D-printed fillable grids that better mimic specific tissue distributions and organ structures (23,30,36,37) analogous to certain practices in radiology. The grid's design parameters can be adjusted to simulate different tissue densities and thus different high-energy photon attenuation characteristics. They also simplify the ability to model complex activity distributions with a single radiotracer injection, as the internal grid structure modulates concentration across various regions, eliminating the need to fill multiple compartments. This minimizes the potential for errors arising from

NOTE: This preprint reports new research that is not certified by peer review and should not be used to guide clinical practice.

the use of multiple radiotracer solutions with varying activity concentrations. Additionally, the design parameters can be adjusted to print features with a resolution considerably lower than the spatial resolution of the scanner (30) and obviate the need for cold walls between the regions of interest. SLA grids of multiple contrasts were studied for SPECT (30,36). Monte Carlo simulations were also used to validate that such studies are compatible with existing practices.

The radiological properties of the printing material have been a key concern, ideally exhibiting a density and x-ray attenuation equivalent to water (5,12). While SLA printing offers high precision and good quality of the surface, mostly resulting from the properties of the resin, the densities of phantoms are typically higher than that of water (30). FDM uses materials such as thermoplastics, like polylactic acid (PLA) or ABS, which tend to be closer to the desired properties (36), making them more radiologically compatible for hybrid imaging applications. In particular, mainly SLA has been explored for grid-based approaches whereas knowledge of FDM's performance in such applications is limited. Also, these grid-based approaches have been focused on SPECT with very little emphasis on PET applications which is reflected in the contrast ratios achieved in these studies compared to current PET detection performance. Unfortunately, most previous designs have been optimized for SPECT or PET, with little consideration given to the dual-modality nature of the hybrid imaging in practice (PET/CT and SPECT/CT). Though previous studies have confirmed that the CT-based PET attenuation correction (CTAC) works for such studies, water neutral attenuation is preferred (23,30,36). Therefore, a standardized approach is needed that accounts for both imaging modalities, leading to a grid design that delivers reliable results in both PET and CT.

We report an investigation of FDM grid-based phantom inserts for PET/CT imaging. Grid spacing, solidity, and different target sizes were investigated as design parameters to balance the trade-off between PET performances without compromising CT attenuation. This work presents a quantitative study of multiple target detectability and quantitation in 3D-printed grid phantoms for PET/CT imaging.

NOTE: This preprint reports new research that is not certified by peer review and should not be used to guide clinical practice.

2. Materials and Methods

2.1. Design and Fabrication of Cubic Grids:

Cubic grids of 4 × 4 × 4 cm were created in Fusion 360 (Autodesk Inc, San Francisco, CA, USA) with the Volumetric Lattice toolset. The 4 cm size was chosen to accommodate the smallest to largest lesions used in conventional QC practices (13). Two essential design characteristics were incorporated: solidity (S) and pore distance (D_P). Solidity is the percentage of solid material that regulates the fillable volume, establishing the contrast between the target and background, while pore distance is the distance between two consecutive pores (a.k.a. base unit cell) which dictates the permeability (ease of volumetric filling by the fluid) and resolution. A key design challenge for the grid is to balance and achieve a suitable trade-off that enhances activity dispersion and movement of air bubbles from the mesh. Three S configurations (50, 60, and 70%) and three D_P variants (5,7,10 mm) were investigated as shown in (**Figure. 1.a**). The target voids of varying diameters (T: 10, 15, and 20 mm) were created by a Boolean subtraction centred on the cubic grids (**Figure. 1.b**) and the spherical shape was chosen because of conventional QC practices. To streamline the design identification, S-D_P-T nomenclature (representing solidity, distance, and target diameter) was used in order to be directly compatible with Fusion 360 as opposed to the fillable volume fraction (FVF) nomenclature previously used by (30). A total of 36 cubes were designed, of which 9 were non-target homogeneous cubes and the other cubes with spherical targets based on the possible permutations of the S-D_P-T. Additionally, a cube holder support (diameter 20 cm, thickness 7 mm) with a 3 × 3 layout for cube insertion was designed to match the internal diameter of a Jaszczak phantom cylinder as shown in (**Figure. 1.c**) in order to fix the cubes within the phantom. This support structure was also meshed with specifications of S=50 %, D_p=7 mm, allowing for the efficient mixing of the radioactive tracer activity and enabling air bubbles to move freely. Gyroid patterns belonging to TMPS (triply minimal periodic structures) family were used for the grid structure, having been found to have good directional fluid permeability compared to other patterns (38). The models after meshing were exported

NOTE: This preprint reports new research that is not certified by peer review and should not be used to guide clinical practice.

as .STL files with a minimum resolution of 0.45 mm and were sliced for printing in a Prusa Slicer (Prusa Research, Prague, Czech Republic). Each set was then 3D-printed with the Prusa MK3S+ Printer (Prusa Research, Prague, Czech Republic) using ABS. ABS is currently the optimal material to emulate water (23) and is typically used for QC test objects, because of its physical and radiological properties. The print parameters used can be found in **Table 1**. To characterize the printing accuracy, the theoretical expected weight for homogeneous cubes based on a 100% solidity cube were calculated. Printed density (ρ) was also calculated from measured weight and design volume (From Fusion 360). 5% maximum deviation was deemed as an acceptable threshold for both weight and density.

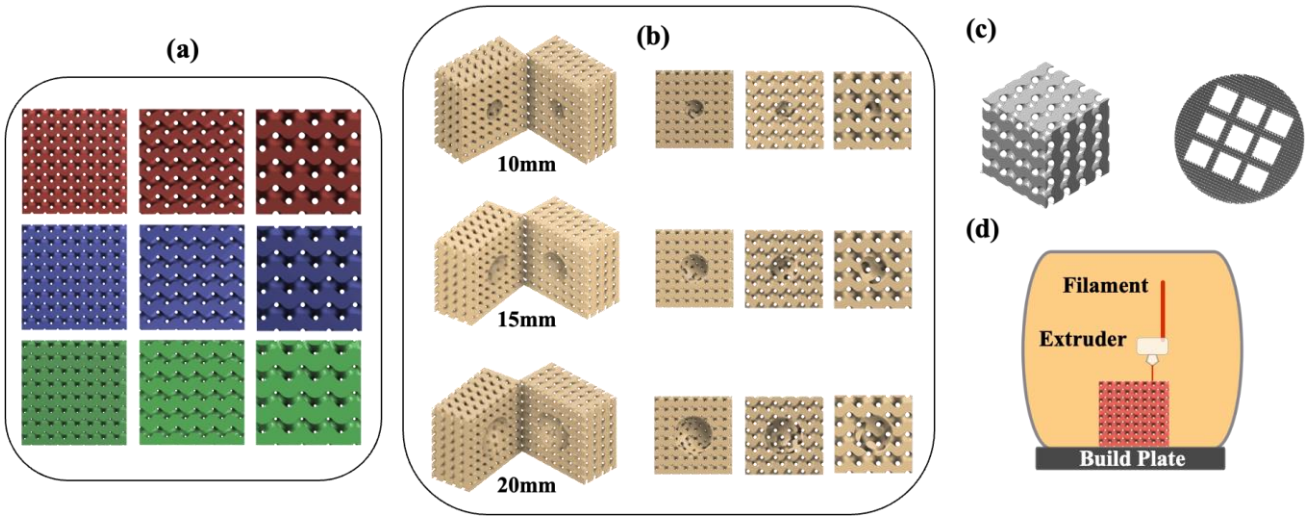

Figure 1. Schematic of grid design and fabrication: (**a**) Central section of baseline 6 design parameters, Rows - *S*: 50% (red), 60% (blue), 70% (green) & Columns – D_P: 5 mm, 7 mm, 10 mm; (**b**) Split cubes and central Slice for varying D_P, showing different targets (*T*: 10 mm, 15mm, 20 mm). (**c**) Rendering of cube insert and designed Jaszczak cube holder used for G-code generation; (**d**) FDM illustration for fabrication of the designed inserts

NOTE: This preprint reports new research that is not certified by peer review and should not be used to guide clinical practice.

Table 1. 3D Printing Parameters used for each set

Print Parameters for the Cubes	
Filament	ABS Plus (eSUN, Shenzen, China)
Infill	100%*
Print Time	3 h (for each cube), 7 h (for each support)
Nozzle Temperature	250 ºC
Bed Temperature	Cubes - 100 ºC
Density	1.01 g/mL
Support	None
*** 100% infill was utilized since the .STL files were already meshed in Fusion 360**	

2.2. Phantom Preparation Protocol – 36 Cube Investigation:

Cubes were positioned within a Jaszczak phantom cylinder as previously mentioned. Thirty-six cubes were arranged in 4 different layers of 9 cubes per layer as per configurations presented in **Figure 1(a)**. The expected contrast ratio (between background solution and the cube) or target-to-background ratio (TBR, between the spherical void and cube) for *S*: 50 %, 60 %, and 70 % is 2, 2.5, and 3.3, respectively. These are much higher than previous SPECT studies (28,30,36). However, the imaged ratio provided by the 3D-printed grid after accounting for printing and imaging artefacts can vary. The simplified phantom preparation protocol is illustrated in **Figure 2**. Phantom filling was facilitated by a mixture of distilled water and soap, which was used to reduce the solution's surface tension (39). The phantom was left for 6 hours with this soap solution to allow trapped air bubbles inside the grids to reach the top, beyond regions of interest. The phantom was filled with water (**Figure 2 a-c**) on Thursday (Day 0) for the initial acquisition, followed by Friday (Day 1). It was left undisturbed over the weekend and subsequently used for three additional consecutive acquisitions from Monday to Wednesday (Days 4-

NOTE: This preprint reports new research that is not certified by peer review and should not be used to guide clinical practice.

6), totalling five acquisitions. Twenty to forty minutes before each acquisition, the radiotracer was injected into the water (volume of 4.5 L) within the phantom. The tracer was administered in a single injection protocol emulating clinical protocols rather than as a prediluted stock solution strategy used for similar phantom studies (**Figure 2 d-f**). The tracer used in this study was [^{18}F] FDG (Fluorodeoxyglucose), as per typical clinical protocols and was injected on each acquisition day as per **Table 2**.

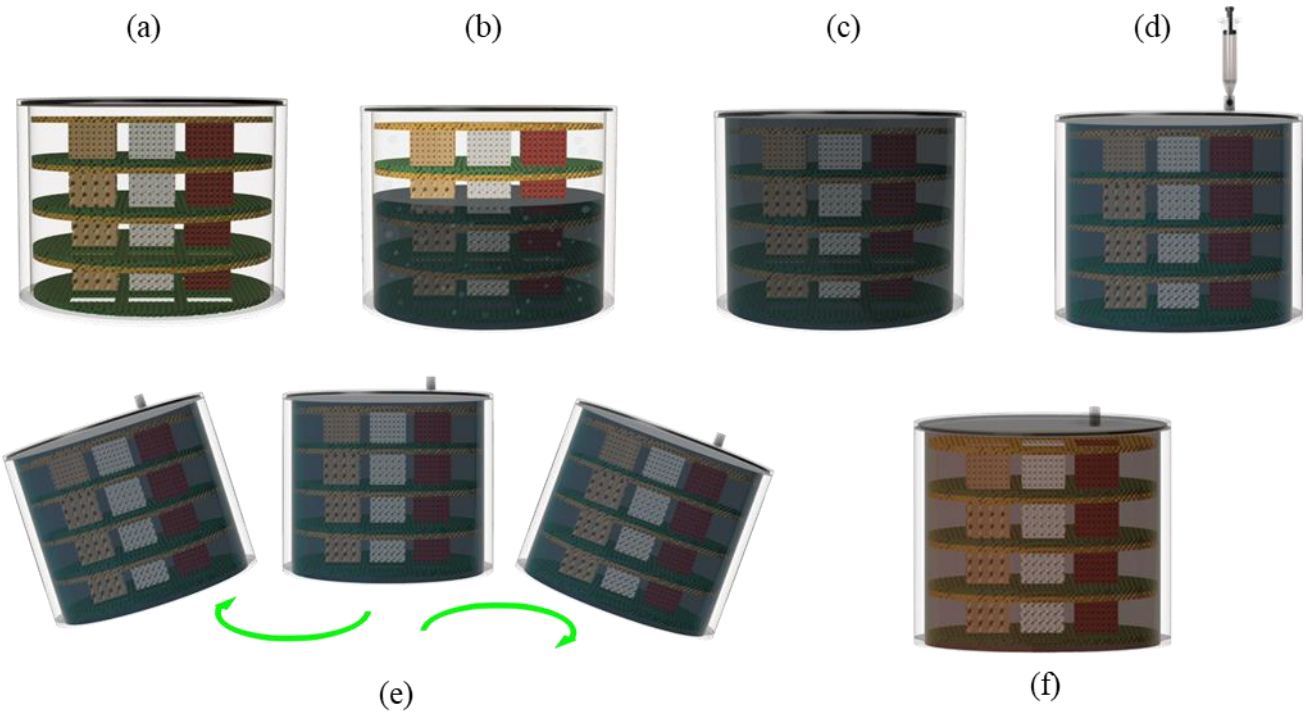

Figure 2. Phantom preparation protocol: (**a**) placement of support & cubes inside the phantom, (**b**) filling phantom with soap water solution, (**c**) phantom relaxation, (**d**) injection of activity, (**e**) mixing post-injection by shaking, (**f**) radioactive phantom ready for imaging

NOTE: This preprint reports new research that is not certified by peer review and should not be used to guide clinical practice.

Table 2. Injected Activity

Acquisition Number	Injected Activity (MBq)	Decay Time (min)	Activity at Acquisition Start (MBq)	Day
1	82.8	60	56.1	0
2	66	73	41.2	1
3	64.3	45	47.5	4
4	60.4	30	47.5	5
5	54.4	25	45.4	6

Table 3. Acquisition Parameters

Acquisition Parameters used for the PET	
Matrix Size	256 × 256
Slice Thickness	2.8 mm
No. of Slices	89
Scan Duration	5 × 300 s
Reconstruction Diameter	600 cm
Pixel Dimensions	2.34 × 2.34 mm
Voxel Dimensions	2.34 × 2.34 × 2.8 mm
Voxel Volume	15.43 mm^3
Reconstruction Algorithm	QCFX (time-of-flight BPL)
Beta	550

*Bayesian penalized-likelihood reconstruction with regularization parameter beta.

NOTE: This preprint reports new research that is not certified by peer review and should not be used to guide clinical practice.

2.3. Imaging & Reconstruction Parameters:

All acquisitions were performed on a Discovery MI 5-ring digital PET-CT system (GE Healthcare, Chicago, IL, USA) (40). CT images were acquired slice thicknesses of 3.75 mm for CTAC, 2.5 mm for CT, and 1.25 mm for high resolution CT, with a pitch of 1.375, current of 89 mA, and peak voltage of 100 kV. The CTAC interval was 2.8 mm to match the PET. For each experimental iteration, 5 consecutive acquisitions of 5 minutes each centred on the phantom were performed. Applied corrections and protocol were similar to that of a clinical setting. Some acquisition parameters used are summarized in **Table 3**.

2.4. Data Extraction and Analysis:

For data assessment, visual comparison of the central axial slices for each cube layer was performed for both CT and PET scans, leading to qualitative proof of concept. The key features observed are the visual changes in the texture of the cubes over time, contrast across features and the visibility of the targets. Subsequently, quantitative data extraction was carried out using image interpretation software PETVCAR® on AWServer client console (GE Healthcare, Chicagio, IL, USA) following the workflow of (13). The three main regions in the DICOM images were classified as background solution, cube mesh, and targets. For each set of images, 36 spherical VOIs corresponding to the true internal volume of the spheres were placed centered on the cubes (For the non – target cubes, VOI size was maintained as per the 20 mm target cubes). Additionally, 4 spherical VOIs were placed for each layer in background adjacent to the cubes and were averaged per layer. Alongside Hounsfield Units (HU) for the CT and activity concentration (kBq/mL) for mean, maximum and standard deviation were extracted. The data extraction led to 1180 measurements of which 180 HU values (*36 cubes across 5 Days)* were from the CT and 1000 activity concentration (900=36 cubes × 5 days × 5 per day and 100= 4 backgrounds × 5 days × 5 per day) values were from the PET. For each day, HU data were averaged in 2 different sets: first as a function of solidity and then as a function of pore distance. The extracted

NOTE: This preprint reports new research that is not certified by peer review and should not be used to guide clinical practice.

PET data for each day was averaged over the respective 5 consecutive acquisitions thus leading to 180 insert VOI values (36 cubes × 5 days) and 20 background values (4 layers × 5 days).

The SUV (standardized uptake value) was then calculated as below with a phantom weight of 4.5 kg, decay corrected to the start of the PET acquisition:

$$\mathrm{SUV}_{(\mathrm{mean\ /\ max})} = \frac{\text{Extracted activity inside ROI in } \frac{\mathrm{Bq}}{\mathrm{mL}} \text{ (mean/max)}}{\text{(Injected activity in Bq)/(weight of phantom in g)}} \quad (1)$$

For analysis, two quantitative metrics were calculated from the SUV data: the recovery coefficient (RC) and dilution coefficient (DC). Both mean and maximum for these metrics were calculated using Equations 2 and 3:

- Recovery coefficient representing the dispersion of activity within the target voids relative to the background water (13).

$$\mathrm{RC}_{(\mathrm{mean/max})} = \frac{\text{SUV inside the target (mean/max)}}{\text{SUV in the background water (mean/max)}} \quad (2)$$

- Dilution coefficient represents the contrast between the printed homogeneous cube and the background water. This is analogous to contrast modulation coefficient in (30) and is only used for non-target cubes

$$\mathrm{DC}_{(\mathrm{mean/max})} = \frac{\text{Activity concentration of the homogeneous cube (mean/max)}}{\text{Activity concentration of the background water (mean/max)}} \quad (3)$$

Theoretical DCs are 0.5, 0.4, and 0.3, corresponding to contrast / TBR of 2, 2.5, and 3.33, respectively. To assess the homogeneity in background activity concentration, SUV values across 4 layers for each day were analyzed and a pairwise errors across layers were calculated. An acceptable threshold of 10% similar to QC uniformity studies (12) was chosen. A subsequent statistical analysis on the dataset of 180 PET metrics ($\mathrm{RC}_{\mathrm{Mean}}$ & $\mathrm{RC}_{\mathrm{Max}}$) was performed for normality through the Shapiro-Wilk test (41) separately on both median and maximal values. The normality tests were complemented by a non-

NOTE: This preprint reports new research that is not certified by peer review and should not be used to guide clinical practice.

parametric counterpart, Friedman Test to assess global consistency across the metrics over 5 days (42). Post hoc analysis the of Wilcoxon signed-rank test (10,43) was performed to investigate the pairwise statistical differences in recovery coefficients between days. All statistical analyses were conducted in Integrated Development Environment for R (RStudio PBC, Boston, MA) with a predetermined significance level of $p < 0.05$.

3. Results:

3.1. Assessment of Printing Accuracy

The 3D-printed cubes had high accuracy in the aspect of weight, with all measurements within 5% of expected. The weight measurements of the cubes on the print day can be found in **Table 4**. The highest deviation of 3.125%, was observed for the 50-10-0 (*S-DP-T*) and 50-7-0 cubes. The density of the printed section of the grids was estimated to be between 0.97 – 1.03 g/mL, which is within 3 % of that of water (reference value: 1.00 g/mL). **Figure 3** illustrates the printing of the cubes, also the results post printing for one of the layers.

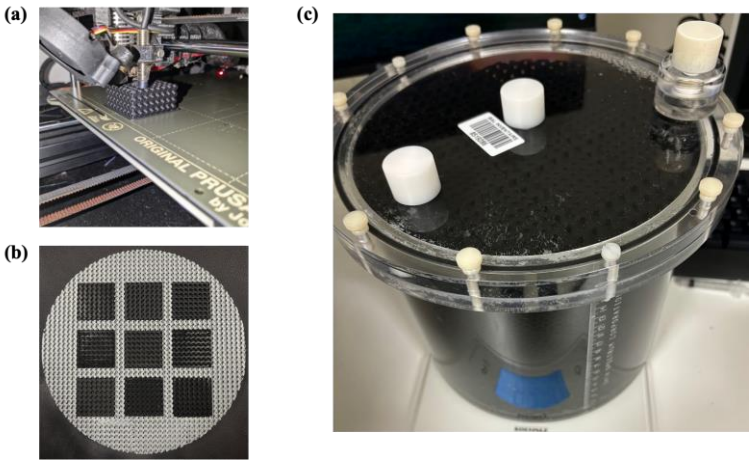

Figure 3. (a) Snapshot of cubes during printing; (b) Printed inserts arranged in a 3 × 3 layout using the cube holder; (c) Assembled Jaszczak phantom post-filling

NOTE: This preprint reports new research that is not certified by peer review and should not be used to guide clinical practice.

Table 4. Measured Weight of 3D-Printed Cubes

Cube (S-D-T)	Measured Weight (g)	Expected Weight (g)	Difference in Weight (%)	Effective Density (g/cc)
100-0-0	64	-	-	-
50-5-0	32	32	0	1.00
50-7-0	33	32	-3.125	1.03
50-10-0	31	32	3.125	0.97
60-5-0	37.5	38.4	2.34	0.98
60-7-0	37.3	38.4	2.86	0.97
60-10-0	38	38.4	1.04	0.99
70-5-0	44	44.8	1.79	0.98
70-7-0	44	44.8	1.79	0.98
70-10-0	44.1	44.8	1.56	0.98

3.2. CT Progression over 5 days:

CT image assessment showed a clear temporal trend among Hounsfield Unit (HU) values. Qualitatively, viewed at the same intensity windowing (width: -40, level: 400; abdominal windowing), CT imaging showed a visual improvement in rendering with prolonged immersion of cubes in that the difference between the cubes and background diminishes **(Figure 4.a)**. For example, the minimum HU value within the VOI's was −40 ± 6 (Day 0, 70-7-0) which increased to −28 ± 5 by Day 6. HU values varied across the cubes, but mean HU values had a trend toward neutral attenuation of water

NOTE: This preprint reports new research that is not certified by peer review and should not be used to guide clinical practice.

(HU = 0) with reduced standard deviations across the days. This trend is illustrated in **Table 5** and **Figure.4b, 4c** for the homogeneous cubes. HU values increased an average 1.5 to 2.7 HU per immersion day depending on the design parameter. A pore distance (D_P) of 5 mm exhibited the most drastic variation in HU values throughout the five-day regimen as seen in **Figure 4.a**.

Table 5. Hounsfield Units values for Homogeneous Cubes

Solidity (%)	**Pore Distance (mm)**	**Hounsfield Units (Mean $\pm$ SD)**				
		Day 0	**Day 1**	**Day 4**	**Day 5**	**Day 6**
50	**5**	−21.4±4.9	−16.6±3.7	−9.8±3.5	−6.4±3.2	−4.4±3.7
	7	−21.5±5.2	−19.3±4.2	−12.9±4.1	−11.6±3.9	−12.1±3.3
	10	−20.5±11.8	−21.1±10	−15.1±8.3	−13.7±7.6	−12.9±6.6
60	**5**	−21.9±3.5	−19.2±3.4	−12.3±3.2	−8.9±3.8	−8.7±3.7
	7	−34.5±9.2	−22.7±9.1	−19.5±9.2	−21.6±7.8	−17.5±8.1
	10	−26.1±11.6	−25.2±11.2	−17.6±8.8	−10.8±7.4	−15.2±7.6
70	**5**	−28.4±4.9	−25.2±3.9	−18.3±4.3	−15.9±4.3	−14.4±3.5
	7	−39.9±5.7	−37.8±5.5	−29.8±5.9	−27.9±4.9	−27.8±4.8
	10	−31.2±7.9	−26.5±8.0	−23.2±8.2	−20.0±8.0	−20.6±7.4

NOTE: This preprint reports new research that is not certified by peer review and should not be used to guide clinical practice.

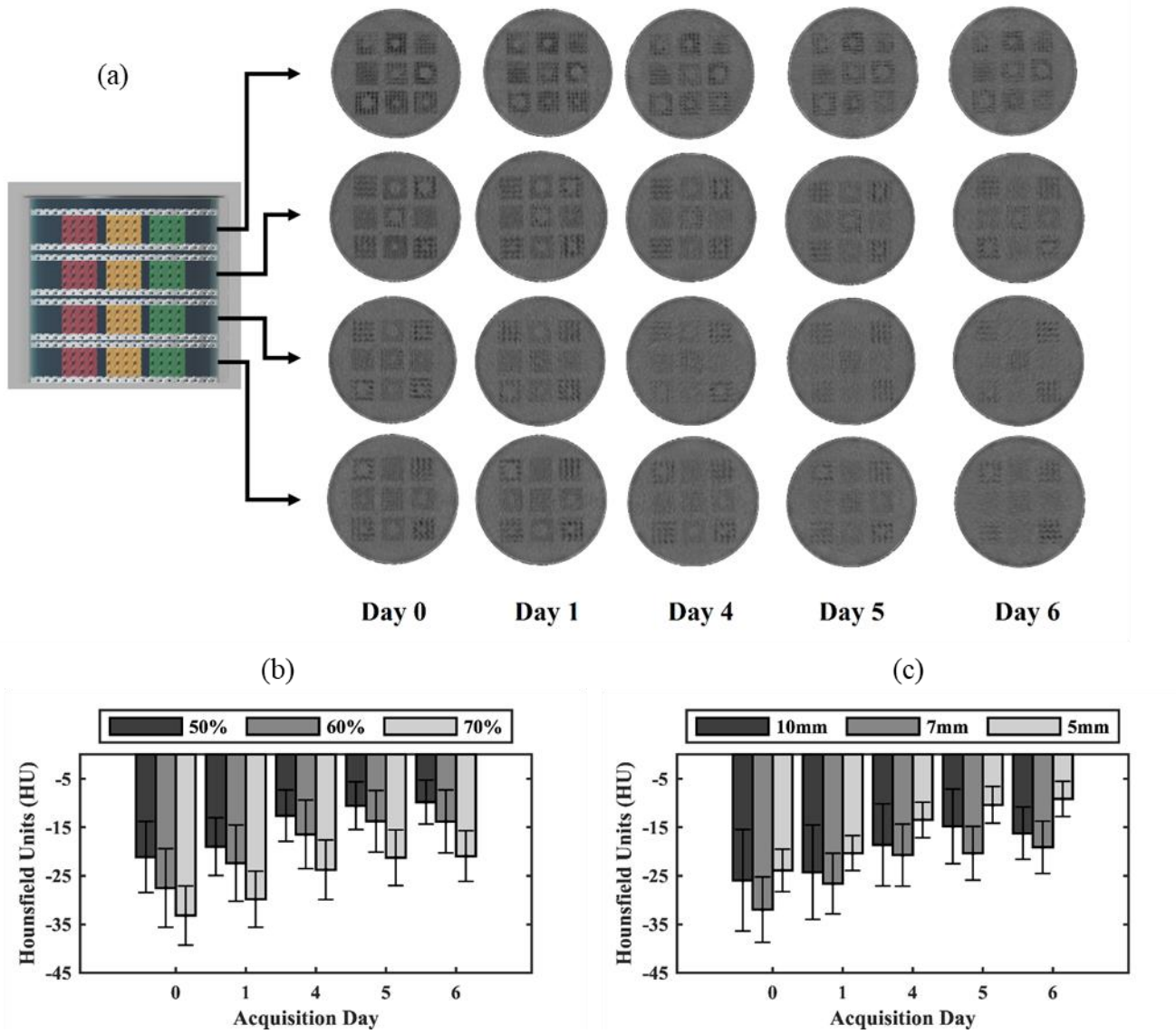

Figure 4. (a) CT progression of central axial slice over 5 acquisition days viewed on abdominal windowing; (b) Averaged HU values as function of pore distance (D_P) and acquisition day; (c) Averaged HU values as function of solidity (S) for homogeneous cubes and acquisition day

3.3. PET Uptake Across Five Days:

Contrast differences in the PET images viewed with the same SUV display window (0-2 g/mL) are illustrated in **Figure 5.a**. Clear demarcation is visible among contrasts between the printed cubes, target voids, and the background water. The targets are all distinguishable, but less so as the size decreases. The 70% solidity cubes are the most distinct, and the 50% solidity cubes are the least distinct

NOTE: This preprint reports new research that is not certified by peer review and should not be used to guide clinical practice.

in terms of visual contrast. Also visually evident is that the activity concentration in the background solution varies between different layers of the phantom. No significant differences apart from this can be seen between days. Dilution coefficient values for the 9 homogeneous cubes are presented in **Figure 5.b**. Dilution coefficients expected for respective solidities are 0.5, 0.4, and 0.3. For 50 % solidity, the dilution coefficients fluctuate around the theoretical value of 0.5, with extreme outliers based on the pore distance and days. For 60 % solidity, the coefficients of dilution range from 0.35 to 0.48, and for 70 % solidity, the dilution coefficients are consistently higher than expected, with values ranging from 0.32 to 0.40. Recovery coefficient mean and maximum values are presented in **Figure 6**. RC values varied over the five acquisition days for all three pore distances 5 mm, 7 mm, and 10 mm but no clear quantitative pattern was seen as function of acquisition day, unlike the CT HU values. The larger spherical targets (20 mm) consistently demonstrated RC values closer to ideal expectations in contrast to the results for the 10 mm targets. The quantitative variability in background SUV_{mean} and SUV_{max} are presented on **Figure 7.a, 7.b.**

Table 6. Summary of Statistical Tests

Statistical Test	Key Results (Significance – 0.05)
Shapiro-Wilk Normality Test	RC_{Max}: W = 0.91, *p-value* <0.05 RC_{Mean}: W = 0.93, *p-value* <0.05 DC_{Max}: W = 0.93, *p-value* <0.05 DC_{Mean}: W = 0.91, *p-value* <0.05
Friedman Test	RC_{Max}: *p-value* = 0.67; RC_{Mean}: *p-value* = 0.93 DC_{Max}: *p-value* = 0.03; DC_{Mean}: *p-value* = 0.07

The results of statistical tests can be found in **Table 6** and **Figure 7.c, 7.d**. All the data was found to be non – normal based on the Shapiro-Wilk Normality Test. Friedman tests show that the deviation in

NOTE: This preprint reports new research that is not certified by peer review and should not be used to guide clinical practice.

normalized values are not statistically significant across days. However, Wilcoxon tests give a statistical difference for combinations with Day-4 for the maximum measurements and Day-6 and Day-4 for the mean measurements.

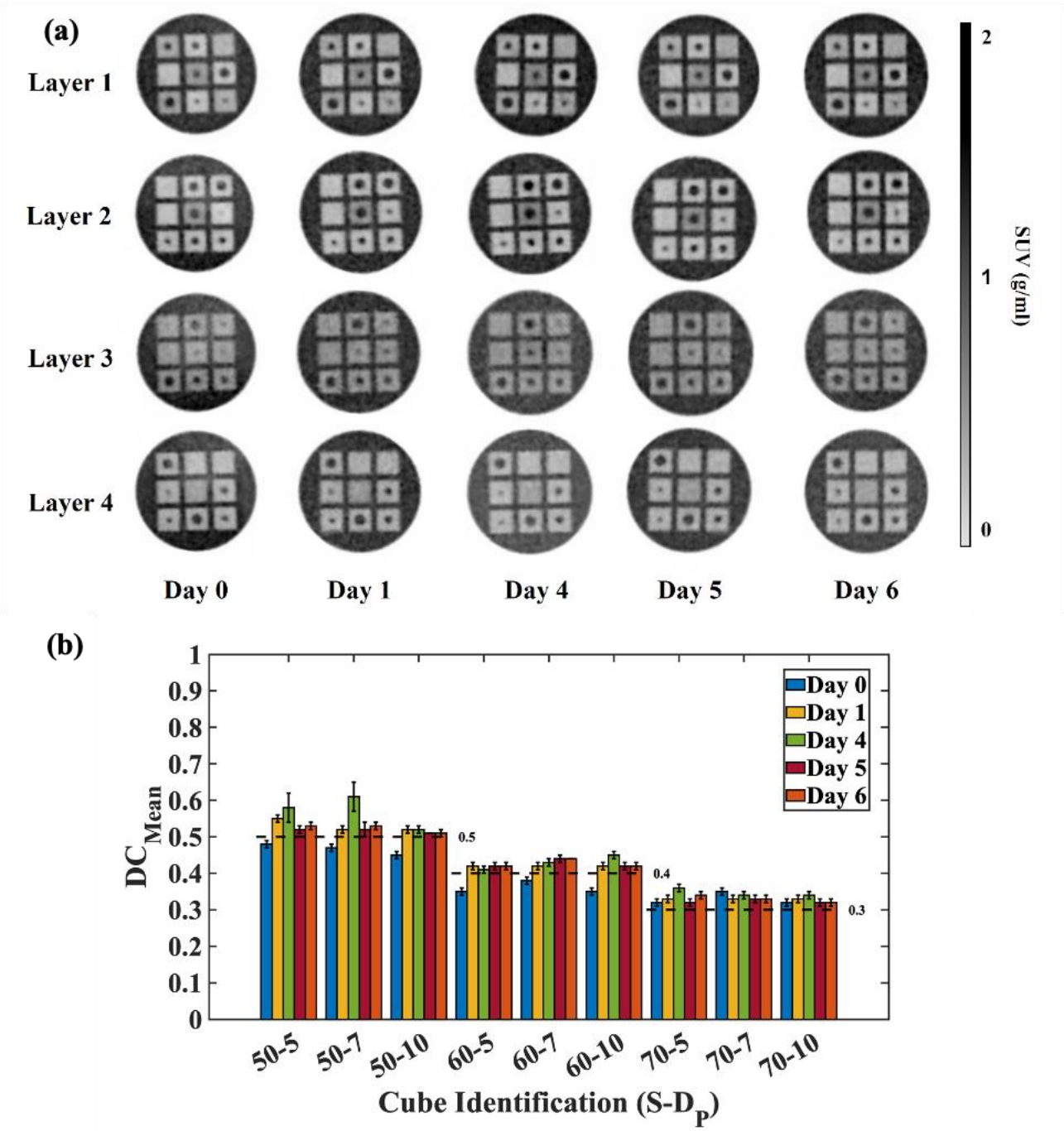

Figure 5. (a) Central axial PET slice for each layer over 5 acquisition days viewed on same SUV window scale; (b) DC_{mean} values as function of pore distance (Corresponding DC_{mean} and DC_{max} data can be found in Table A1)

NOTE: This preprint reports new research that is not certified by peer review (Currently submitted for review to Physics in Medicine) and should not be used to guide clinical practice.

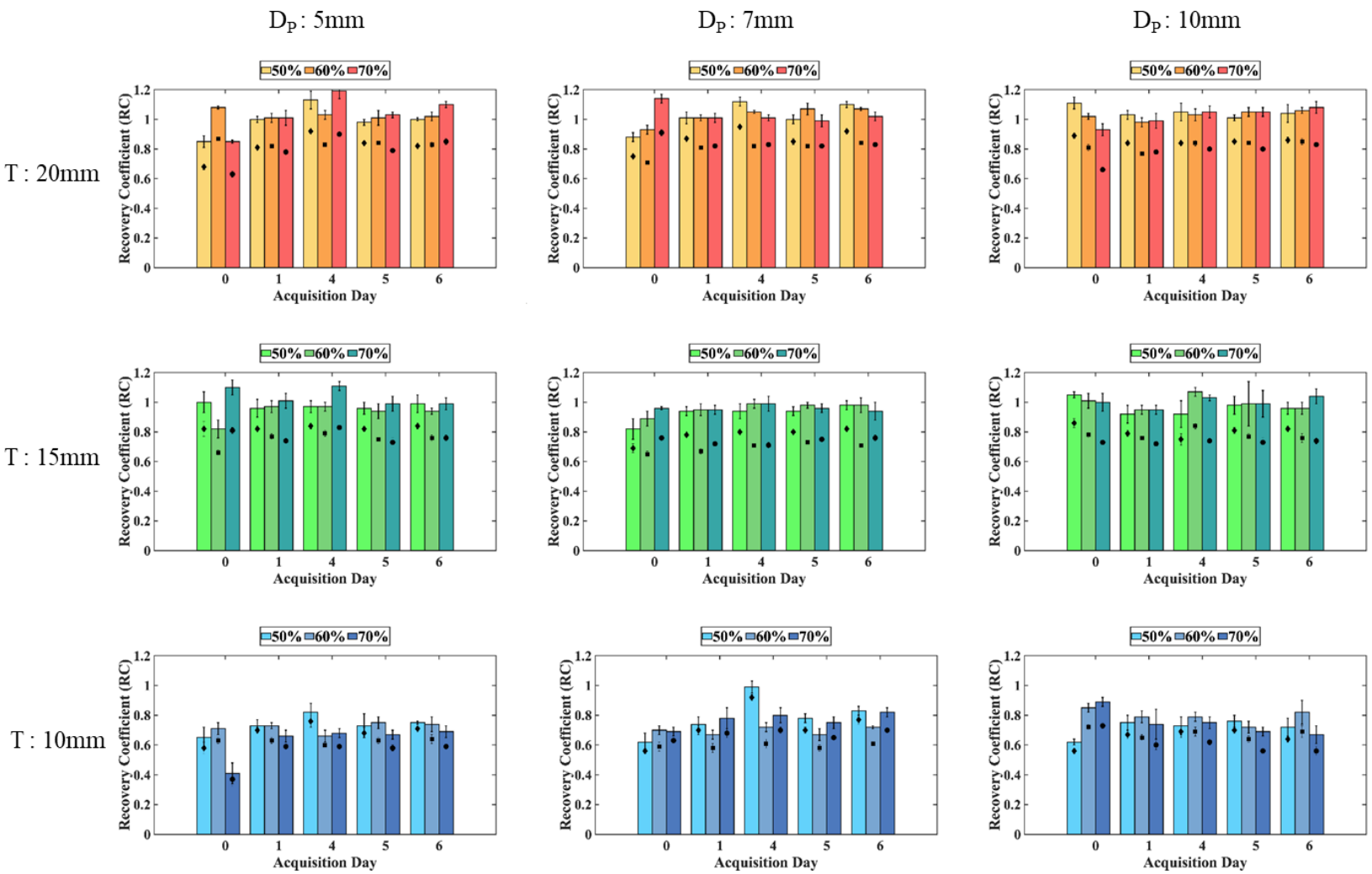

Figure 6. Recovery coefficient bar plots for the 36 cube study as function of solidity (*S*) and pore distance (D_P) over different acquisition days; The bars represent RC_{max} with error bars and the filled markers inside the bar plots represent corresponding RC_{mean}. The figure is arranged as rows (targets: 20, 15, 10 mm) and columns (pore distance: 5, 7, 10 mm). (Corresponding data can be found in Tables A2, A3 & A4)

NOTE: This preprint reports new research that is not certified by peer review and should not be used to guide clinical practice.

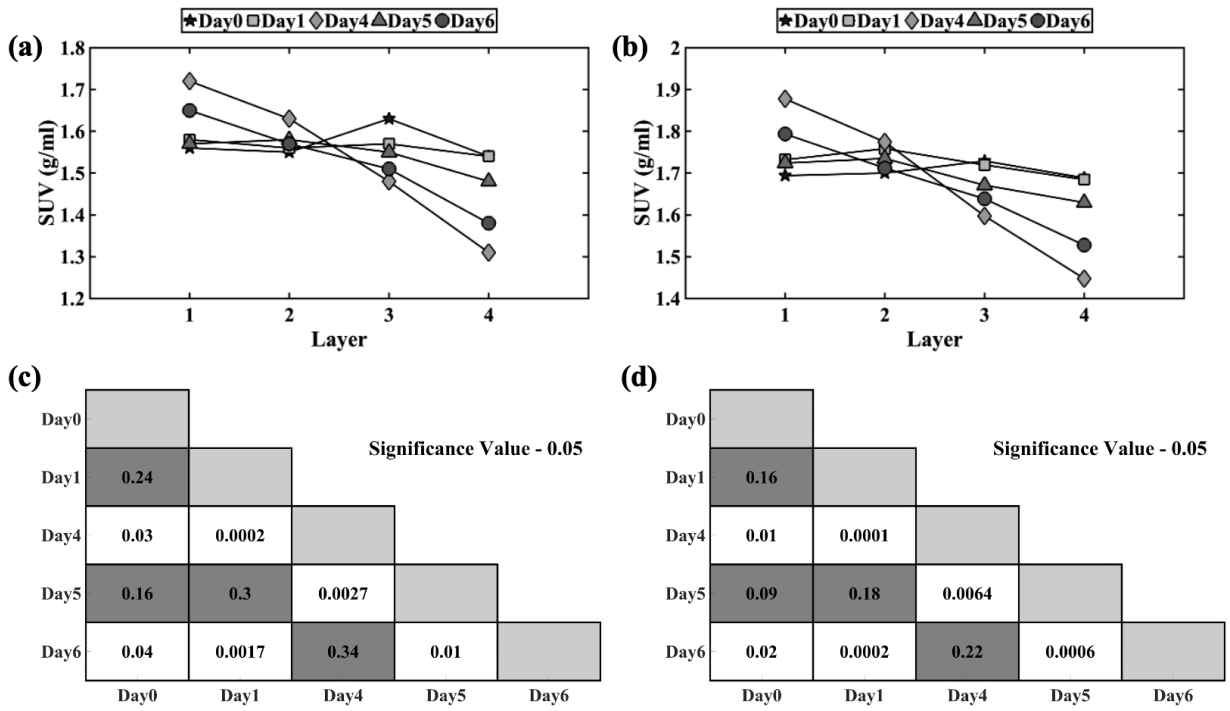

Figure 7. SUV variation across 4 layers (a) SUV_{Mean} (b) SUV_{Max}; Wilcoxon signed-rank test p – value matrix for (c) RC_{Max} and (d) RC_{Mean} - White represents combinations that have statistical differences

4. Discussion:

Low Cost FDM based 3D-printed cubic inserts were explored as a possible alternative to acrylic spheres to create targets in PET/CT QC phantoms. Printing accuracy of the cubes weighing between ± 5% of expectation indicates the accuracy of FDM in the production of phantom inserts with a precision crucial for the true representation of the planned experimental setup. These also fall within the prescribed thresholds of previous 3D printing-based studies (30,36). The equivalent density of the solid component (0.97 – 1.03 g/cc) falls within the range of water which is a beneficial property for neutral attenuation compared to most tissue. It should be noted that reproducibility of FDM can be subject to various factors, such as material behavior, print conditions and design complexity. One such design limitation in this study was the pore distance which had to be limited to 5 mm considering the printer's resolution.

NOTE: This preprint reports new research that is not certified by peer review and should not be used to guide clinical practice.

From the PET/CT, the temporal pattern shift observed in Hounsfield Unit (HU) measurements on the CT over the course of the seven-day immersion period strongly suggests a dynamic interaction between the ABS material and the surrounding water environment. Qualitative and quantitative enhancement in the image rendering with respect to HU measurements confirms the role of the printing inaccuracies of FDM. The water molecules, as they fill up the available air spaces due to printing defects cause a rise in the bulk density of the material itself during the scan (44,45). Additionally, this very process could also be responsible for causing a reallocation of the electron density in the material contributing to change in HU values. Hence, temporal CT attenuation changes necessitate special attention to the history of immersion for 3D-printed phantom inserts.

PET images presented a contrast picture with no appreciable qualitative or quantitative evidence for the same phenomenon. A plausible explanation is that the injection of the radiotracer performed every acquisition day prior to scanning, limits the time window during which there may be significant material changes to manifest in the PET data. For a full exploration of the effect on PET, future studies using radiotracers with longer half-lives than used in this work are recommended. One of the parameters which is not explicitly mentioned in this work is the pore size which reduces in proportion with pore distance. Lower pore distances within same solidity can lead to pore sizes lower than the resolution of both CT and PET making them qualitatively invisible on the images (30). A limitation in this regard is that a threshold for D_P that could account for fluid permeability and scanner spatial resolution to optimize quantitative performance has yet to be determined. Thus, a future dataset optimization on D_P can enable anthropomorphic studies like (30,36) with FDM to reduce the gap between phantom and clinical reality. Evident visible contrast variations in the PET images verified that the scanner could indeed distinguish three regions: the printed cubes, target voids, and background water. This is essential for the accurate quantification of radiotracer uptake. The fact that the 70 % solidity cubes had the maximum visual contrast, whereas 50% solidity cubes had the minimum visible contrast, highlights that the increased solidity causes a reduction in the average of activity within the

NOTE: This preprint reports new research that is not certified by peer review and should not be used to guide clinical practice.

cubes, resulting in better contrast. As the target size reduces, the visibility becomes more limited as mentioned by (13). Quantitative metrics show a comparable recovery coefficient to that of walled spheres of similar ratios (10). Recovery coefficients were consistent across days and no significant statistical differences were observed globally as per Freidman tests (**Table 7**). The recovery coefficients also highlighted the complexity of tracer distribution and quantification in FDM-printed inserts. For a D_P of 5 mm, 69% of RC_{max} values and 39% of RC_{mean} values yielded greater than 80% recovery. For a D_P of 7 mm, 62% of the RC_{max} values and 32% of the RC_{mean} values exceeded same threshold and for D_P: 10mm, the distribution observed was 65% for RC_{max} and 36% for the RC_{mean}. This indicates that the proportions of RC_{max} and RC_{mean} values greater than 0.8 (46) were consistent for all D_P conditions, implying that the pore distance, within the range tested, did not have a significant influence on the overall tracer recovery. This is in line with previous studies (30), in that the fillable volume fraction (solidity) of the printed inserts is the key factor driving PET performance. The measured contrasts averaged on all data as function of solidity were 1.93 ± 0.14, 2.44 ± 0.2 & 3.01 ± 0.08 compared to the theoretical contrasts of 2, 2.5 and 3.33. Additionally, individual DC_{mean} and DC_{max} values (**Figure 5b, Table A1**) indicated a slight systematic bias in measured contrast compared to theoretical values. DC values of 50% cubes from Day 4 due had extreme outliers (Figure 5b) due to non-homogenous mixing which led to statistically significant p values. We performed a retest excluding day 4 DC, which resulted in friedman p values of (DC_{Max}: 0.27) and (DC_{Mean}: 0.11). Although globally the achieved contrast is within the thresholds, the precise value for each experiment can vary, which is in agreement with similar studies (30,36).

The proposed protocol in this study requires one injection of activity in a prefilled phantom rather than a stock prediluted strategy used previously by (28). This was specifically designed to follow the CT in conjunction with PET consistency on multiple days. Another advantage to the proposed protocol is consideration of the methods sensitivity to air bubble, which has been a issue in previous studies (28,30). Because of its prolonged immersion strategy, the proposed protocol had no air bubbles visible

NOTE: This preprint reports new research that is not certified by peer review and should not be used to guide clinical practice.

at the scan resolutions and the HU values were close to that of water, indicating minimal air present in the averages (**Table 5**). However, relying on a single injection of activity can increase the susceptibility to diffusion discrepancies causing a SUV distribution variability along the phantom. Non-uniformity of the activity dispersion in background across phantom layers was apparent as seen in **Figure 5**. The layer variation for Day-4 and Day-6 values fail the 10% threshold as seen in **Figure A2, A3.** Ideally, this should not affect TBR, RC and DC measurements since they are locally normalized to the background at each layer, but a 31 % drop in activity concentration (Figure A3.c) would be accompanied by a 17 % increase in Poisson noise. The injected activity and initial decay time **Table 2** were not the same for various days hence metrics with normalization were used. While local normalization reduced these discrepancies as seen in global *p* values of the Friedman tests, the significance of SUV variation on the metrics is highlighted by the pairwise *p* value maps from the Wilcoxon tests observed in **Figure 7** in which the *p* values decrease significantly for combinations with Day – 6 and Day – 4. To address this comprehensively, a robust preparation protocol and a larger 3D-printed dataset would be necessary in order to optimize design parameters to more closely correlate the contrast ratios to theoretical values. For future studies, removing volume of background solution (example 10 mL) close to the filling cap of the phantom prior to the shaking step and adding it back prior to scan (5,12,47) could reduce the layer to layer variation.

The biggest finding in this study is that 36 targets can be analyzed at once rather than 6 fixed targets in a conventional experimental setup. In terms of impact, this could be reflected as 6 times fewer experiments for the same target sizes and a corresponding reduction in radiation exposure during phantom loading. This reduction factor would depend on the number of target sizes of interest. Another goal of this study was to demonstrate the wall-less effect compared to acrylic spheres. The SUV profile of select cubes from Day 1 and Day 5; (70-5) shown in **Figure A4** is comparable to that of profiles from (10). We see a flat line as expected for non-target cubes, and a peak whose width and height varies with target size for targeted cubes. Since the phantom has 3 different regions, leading to 2

NOTE: This preprint reports new research that is not certified by peer review and should not be used to guide clinical practice.

regional transitions, this can be clearly observed on the SUV profile where target to cube is observed followed by cube to water. A key limitation of this study is the manual data extraction using actual physical volume of the target as the VOI volume, leading to uptake underestimation due to spillover (partial volume effects). While this extraction method worked for walled spheres previously (13), because there is no explicitly distinguishable wall on either CT or PET, it becomes difficult to accurately delineate the targets within the printed cubes. The high number of targets (36) increase the likelihood of manual errors compared to simpler phantoms. This is one of the reasons why the target contrast with respect to the native cube background were not included in this study. Hence, a more consistent automated measurement method accounting for printing inaccuracies and partial volume effects would be necessary for robust data and TBR analysis in future studies. Further, to perform any such multi acquisition comparison studies, the combination of effective activity at scan and pairwise layer variability is more important than pairwise statistical p values. Therefore, through such multi-criteria standards, we can ensure conclusions that are both statistically and practically meaningful.

Significant contribution of this study is the cost of the inserts, each insert and cube holder on average costed less than 5 Euros (estimated by Prusa slicer). Additionally, other costs such as the printer, material, electricity consumption which would total to an overall cost of less than 1000 Euros which is considerably lower than (30). Beyond these points, dimensional inaccuracies resulting from material shrinkage and warping during printing, especially for ABS make the standardization challenging across printers. Also, printing ABS demands for an enclosure to avoid harmful toxicity which may limit usage in hospitals. While equally priced to FDM, generic SLA resins are less ideal for dual-modality imaging since they lack the ability to fulfill the needs of CT. It should be noted that alternative new age SLA resins or low density FDM filaments used have potential for greater resolution whilst maintaining neutral attenuation. Though they come at a relatively higher cost, the overall production cost is significantly lower than industrial polyjet printing (19,27,30). The choice of the 3D-printed insert design for any such studies must be informed by the main aim: if the concern is only about PET

NOTE: This preprint reports new research that is not certified by peer review and should not be used to guide clinical practice.

performance, fillable volume (solidity) optimization is the main priority. However, if enhanced CT performance concurrent with PET performance is required, then the material used, and D_P become the critical design parameters. To expand on this, use of walled spheres without neutral attenuation makes them visible on CT but causes PET edge artefacts. Ideally, to effectively challenge new age PET/CT reconstruction algorithms and analysis software's, lesions that are *not explicitly* visible on CT but *only on* PET could be of great advantage. This would enable one to study activity concentration changes without anatomical cues from the CT. Furthermore, in this study we reproduced conventional practices with the 3D printing of homogeneous regions and spherical targets. A major advantage for further 3D printing backed grid-based studies is its inherent capability to also create heterogeneity, for example creating a second grid within the target void. Besides, anthropomorphic lesions (34,35), which are directly segmented out of patient scans, can be translated into grid-based insert designs, effectively simulating patient-specific anatomy and activity distributions. Pore distance becomes equally important along with solidity as the studies move closer to emulating clinical results. While this study has identified some of the limitations, such as potential biases due to printing or phantom preparation, the major benefits of grid-based approach far outweigh these limitations. With the development of more comprehensive datasets for a wider range of design parameters and printing conditions, these limitations could likely be overcome. Therefore, we conclude that FDM based ABS inserts for PET/CT produce consistent results which are both reliable and reproducible whilst comparable to that of SLA grids and can be extended for more anthropomorphic studies.

NOTE: This preprint reports new research that is not certified by peer review and should not be used to guide clinical practice.

5. Conclusion:

Feasibility of FDM based 3D-printed inserts was established for PET/CT applications. The quantitative metrics were found to be consistent globally across several acquisitions. A single injection protocol with buffer decay time was used instead of pre-diluted stock solution which reduced sensitivity to air bubbles but introduce activity diffusion bias which can be corrected. Further to summarize, the main contributions from this study are as follows

1. Simplified phantom preparation protocol with attendant reduction in radiation exposure
2. Balancing the dual nature of PET/CT
3. Increasing the number of targets scanned per experiment
4. Demonstration of the wall-free effect
5. Reduced costs of 3D-printed inserts

These results open the ground for exploiting FDM based printing for more clinically relevant geometries and activity concentration profiles.

NOTE: This preprint reports new research that is not certified by peer review and should not be used to guide clinical practice.

Abbreviations used in this article are:

ABS	Acrylonitrile Butadiene Styrene
A	Activity Concentration in kBq/ml
DC	Dilution Coefficient
DMI	Discovery MI
D_P	Distance between pores
FDM	Fused Deposition Modelling
FDG	Fluorodeoxyglucose
FOV	Field of View
HU	Hounsfield Units
IEC	International Electrotechnical Commission
NEMA	National Electrical Manufacturing Association
NM	Nuclear Medicine
PET / CT	Positron Emission Tomography / Computed Tomography
PLA	Poly Lactic Acid
QC	Quality Control
RC	Recovery Coefficient
S	Solidity
SD	Standard Deviation
SLA	Stereolithography
SPECT/CT	Single Photon Emission Computed Tomography / Computed Tomography
SUV	Standardized Uptake Value
TOF	Time of Flight
TBR	Target to Background Ratio
TMPS	Triply Minimal Periodic Structures
VOI	Volume of Interest

NOTE: This preprint reports new research that is not certified by peer review and should not be used to guide clinical practice.

Appendix / Additional Files

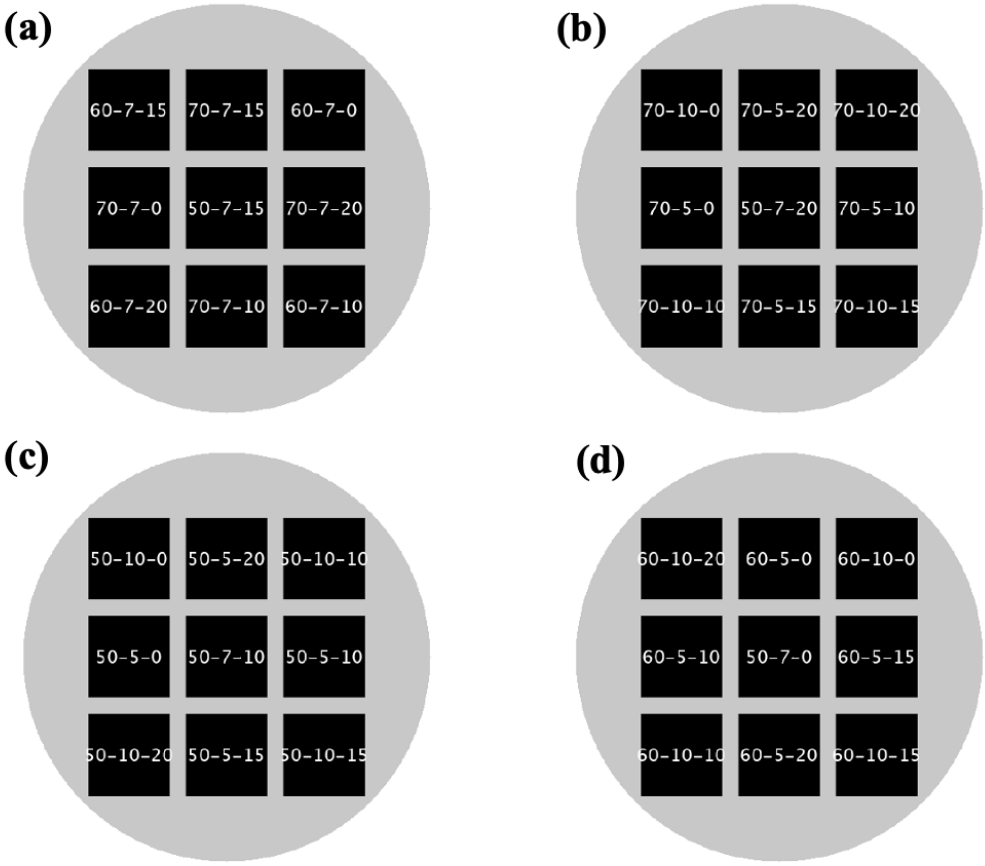

Figure A1. Layout of the 36 Cubes inside the phantom subdivided into 4 Layers – (a) Layer 1, (b) Layer 2, (c) Layer 3, (d) Layer 4

Table A1. Dilution Coefficient values for Homogeneous Cubes

Solidity %	Pore Distance mm	Dilution Coefficient (Max ± *SD* & Mean ± *SD*)				
		Day 0	Day 1	Day 4	Day 5	Day 6
50	5	0.51±0.01 0.48±0.01	0.58±0.01 0.55±0.01	0.64±0.04 0.58±0.01	0.59±0.02 0.52±0.01	0.59±0.00 0.53±0.00
	7	0.49±0.01 0.47±0.01	0.54±0.01 0.52±0.01	0.67±0.04 0.61±0.04	0.54±0.01 0.52±0.02	0.54±0.01 0.53±0.01
	10	0.50±0.01 0.45±0.01	0.56±0.02 0.52±0.01	0.55±0.02 0.52±0.01	0.55±0.02 0.51±0.00	0.53±0.02 0.51±0.01
60	5	0.38±0.02 0.35±0.01	0.45±0.02 0.41±0.01	0.45±0.01 0.41±0.01	0.44±0.01 0.42±0.01	0.44±0.01 0.42±0.01
	7	0.42±0.01 0.38±0.01	0.44±0.01 0.42±0.01	0.44±0.01 0.43±0.01	0.45±0.01 0.44±0.01	0.46±0.02 0.44±0.00
	10	0.38±0.02 0.35±0.01	0.48±0.02 0.42±0.01	0.48±0.02 0.45±0.01	0.44±0.02 0.42±0.01	0.44±0.02 0.42±0.01
70	5	0.34±0.02 0.32±0.01	0.35±0.02 0.33±0.01	0.40±0.02 0.36±0.01	0.34±0.01 0.32±0.01	0.37±0.02 0.34±0.01
	7	0.36±0.01 0.35±0.01	0.36±0.02 0.33±0.01	0.36±0.01 0.34±0.01	0.36±0.02 0.33±0.01	0.36±0.01 0.33±0.01
	10	0.33±0.01 0.32±0.01	0.35±0.01 0.33±0.01	0.38±0.02 0.34±0.01	0.36±0.03 0.32±0.01	0.34±0.01 0.32±0.01

NOTE: This preprint reports new research that is not certified by peer review and should not be used to guide clinical practice.

Table A2. Recovery Coefficient values for Target Cubes (D_P: 5mm)

Solidity %	Target Size mm	Recovery Coefficient (Max ± *SD* & Mean ± *SD*)				
		Day 0	Day 1	Day 4	Day 5	Day 6
50	20	0.85±0.04 0.68±0.02	1.00±0.02 0.82±0.01	1.13±0.06 0.92±0.01	0.98±0.02 0.84±0.01	1.00±0.01 0.82±0.01
	15	1 ± 0.07 0.82±0.05	0.96±0.06 0.82±0.02	0.97±0.04 0.84±0.02	0.96±0.04 0.82±0.01	0.99±0.06 0.84±0.02
	10	0.65±0.07 0.58±0.04	0.73±0.04 0.70±0.02	0.82±0.06 0.76±0.04	0.73±0.08 0.68±0.04	0.75±0.01 0.71±0.01
60	20	1.08±0.01 0.87±0.01	1.01±0.03 0.82±0.01	1.03±0.03 0.83±0.01	1.01±0.05 0.84±0.01	1.02±0.03 0.83±0.02
	15	0.82±0.06 0.66±0.02	0.97±0.04 0.77±0.02	0.97±0.03 0.79±0.02	0.94±0.05 0.75±0.01	0.94±0.02 0.76±0.02
	10	0.71±0.04 0.63±0.02	0.73±0.02 0.63±0.01	0.66±0.04 0.60±0.01	0.75±0.04 0.63±0.02	0.74±0.05 0.64±0.03
70	20	0.85±0.01 0.63±0.02	1.01±0.05 0.78±0.02	1.19±0.05 0.90±0.01	1.03±0.02 0.79±0.01	1.10±0.02 0.85±0.02
	15	1.10±0.05 0.81±0.02	1.01±0.05 0.74±0.01	1.11±0.03 0.83±0.01	0.99±0.05 0.73±0.03	0.99±0.04 0.76±0.02
	10	0.41±0.07 0.37±0.05	0.66±0.04 0.59±0.01	0.68±0.03 0.59±0.01	0.67±0.03 0.58±0.02	0.69±0.04 0.59±0.01

Table A3. Recovery Coefficient values for Target Cubes (D_P: 7 mm)

Solidity %	Target Size mm	Recovery Coefficient (Max ± *SD* & Mean ± *SD*)				
		Day 0	Day 1	Day 4	Day 5	Day 6
50	20	0.88±0.03 0.75±0.01	1.01±0.04 0.87±0.01	1.12±0.03 0.95±0.01	1 ± 0.03 0.85±0.02	1.10±0.02 0.92±0.01
	15	0.82±0.07 0.69±0.03	0.94±0.03 0.78±0.01	0.94±0.05 0.80±0.01	0.94±0.03 0.80±0.01	0.98±0.03 0.82±0.02
	10	0.62±0.06 0.56±0.02	0.74±0.05 0.70±0.03	0.99±0.04 0.92±0.02	0.78±0.03 0.70±0.02	0.83±0.03 0.77±0.03
60	20	0.93±0.03 0.71±0.01	1.01±0.02 0.81±0.01	1.05±0.01 0.82±0.01	1.07±0.04 0.82±0.01	1.07±0.01 0.84±0.01
	15	0.89±0.05 0.65±0.02	0.95±0.04 0.67±0.02	0.99±0.03 0.71±0.00	0.98±0.02 0.73±0.01	0.98±0.05 0.71±0.01
	10	0.70±0.03 0.59±0.01	0.67±0.03 0.58±0.02	0.72±0.03 0.61±0.01	0.67±0.04 0.58±0.02	0.72±0.01 0.61±0.00
70	20	1.14±0.03 0.91±0.02	1.01±0.03 0.82±0.01	1.01±0.02 0.83±0.01	0.99±0.04 0.82±0.01	1.02±0.03 0.83±0.01
	15	0.96±0.01 0.76±0.01	0.95±0.03 0.72±0.01	0.99±0.05 0.71±0.02	0.96±0.03 0.75±0.01	0.94±0.06 0.76±0.02
	10	0.69±0.02 0.63±0.01	0.78±0.01 0.68±0.03	0.80±0.05 0.70±0.02	0.75±0.04 0.65±0.01	0.82±0.03 0.70±0.01

Table A4. Recovery Coefficient values for Target Cubes (D_P: 10mm)

Solidity %	Target Size mm	Recovery Coefficient (Max ± *SD* & Mean± *SD*)				
		Day 0	Day 1	Day 4	Day 5	Day 6
50	20	1.11±0.04 0.89±0.02	1.03±0.03 0.84±0.01	1.05±0.06 0.84±0.01	1.01±0.02 0.85±0.01	1.04±0.06 0.86±0.02
	15	1.05±0.02 0.86±0.03	0.92±0.06 0.79±0.02	0.92±0.09 0.75±0.04	0.98±0.06 0.81±0.02	0.96±0.04 0.82±0.02
	10	0.62±0.02 0.56±0.01	0.75±0.05 0.67±0.03	0.73±0.06 0.69±0.04	0.76±0.04 0.70±0.02	0.72±0.06 0.64±0.02
60	20	1.02±0.02 0.81±0.02	0.98±0.03 0.77±0.01	1.03±0.04 0.84±0.02	1.05±0.03 0.84±0.01	1.06±0.02 0.85±0.02
	15	1.01±0.02 0.78±0.02	0.95±0.06 0.76±0.01	1.07±0.03 0.84±0.02	0.99±0.15 0.77±0.02	0.96±0.04 0.76±0.03
	10	0.85±0.03 0.72±0.02	0.79±0.04 0.65±0.05	0.79±0.03 0.69±0.03	0.72±0.04 0.64±0.02	0.82±0.08 0.69±0.04
70	20	0.93±0.04 0.66±0.02	0.99±0.05 0.78±0.01	1.05±0.04 0.80±0.00	1.05±0.03 0.80±0.01	1.08±0.04 0.83±0.01
	15	1.00±0.06 0.73±0.01	0.95±0.03 0.72±0.01	1.03±0.02 0.74±0.01	0.99±0.09 0.73±0.03	1.04±0.05 0.74±0.02
	10	0.89±0.03 0.73±0.02	0.74±0.09 0.60±0.03	0.75±0.04 0.62±0.02	0.69±0.03 0.56±0.02	0.67±0.06 0.56±0.03

NOTE: This preprint reports new research that is not certified by peer review and should not be used to guide clinical practice.

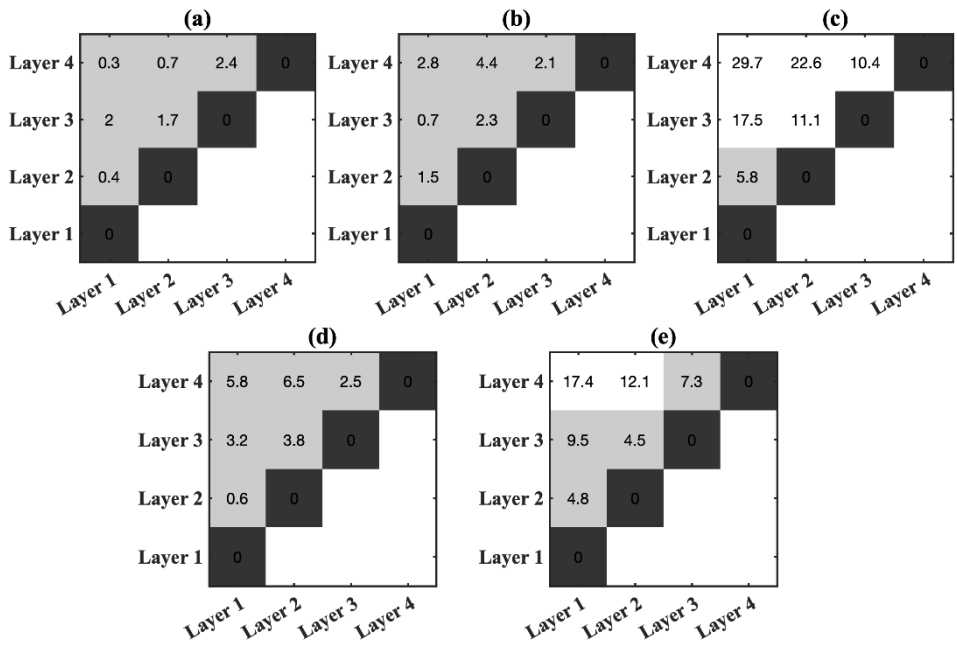

Figure A2. Pairwise SUV_{Mean} Percentage variability matrix for (a) Day 0, (b) Day 1, (c) Day 4, (d) Day 5, (e) Day 6 – White represents the Paris that fail the 10% threshold

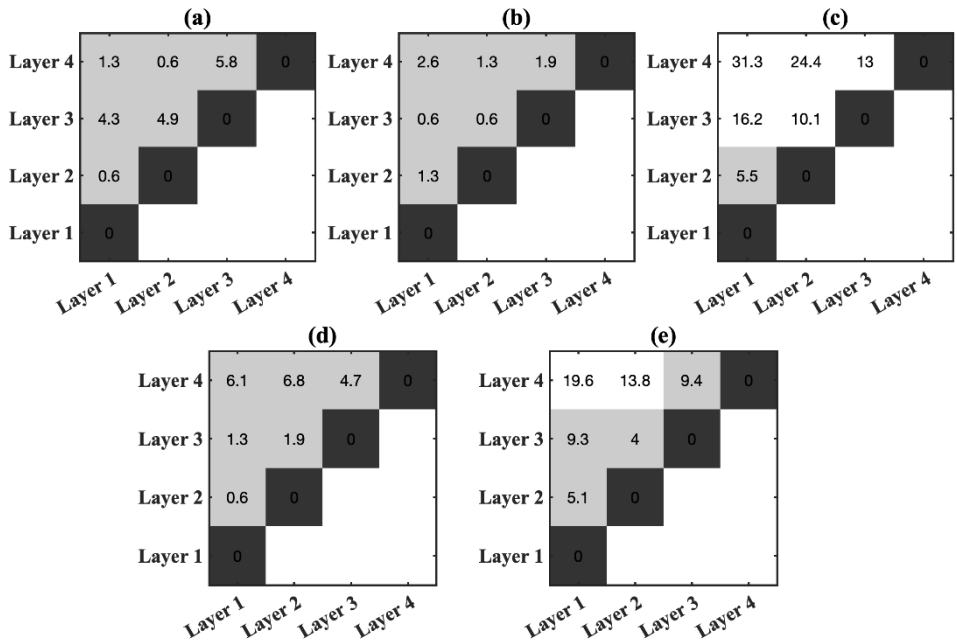

Figure A3. Pairwise SUV_{Max} Percentage variability matrix for (a) Day 0, (b) Day 1, (c) Day 4, (d) Day 5, (e) Day 6 – White represents the pairs that fail the 10% threshold

NOTE: This preprint reports new research that is not certified by peer review and should not be used to guide clinical practice.

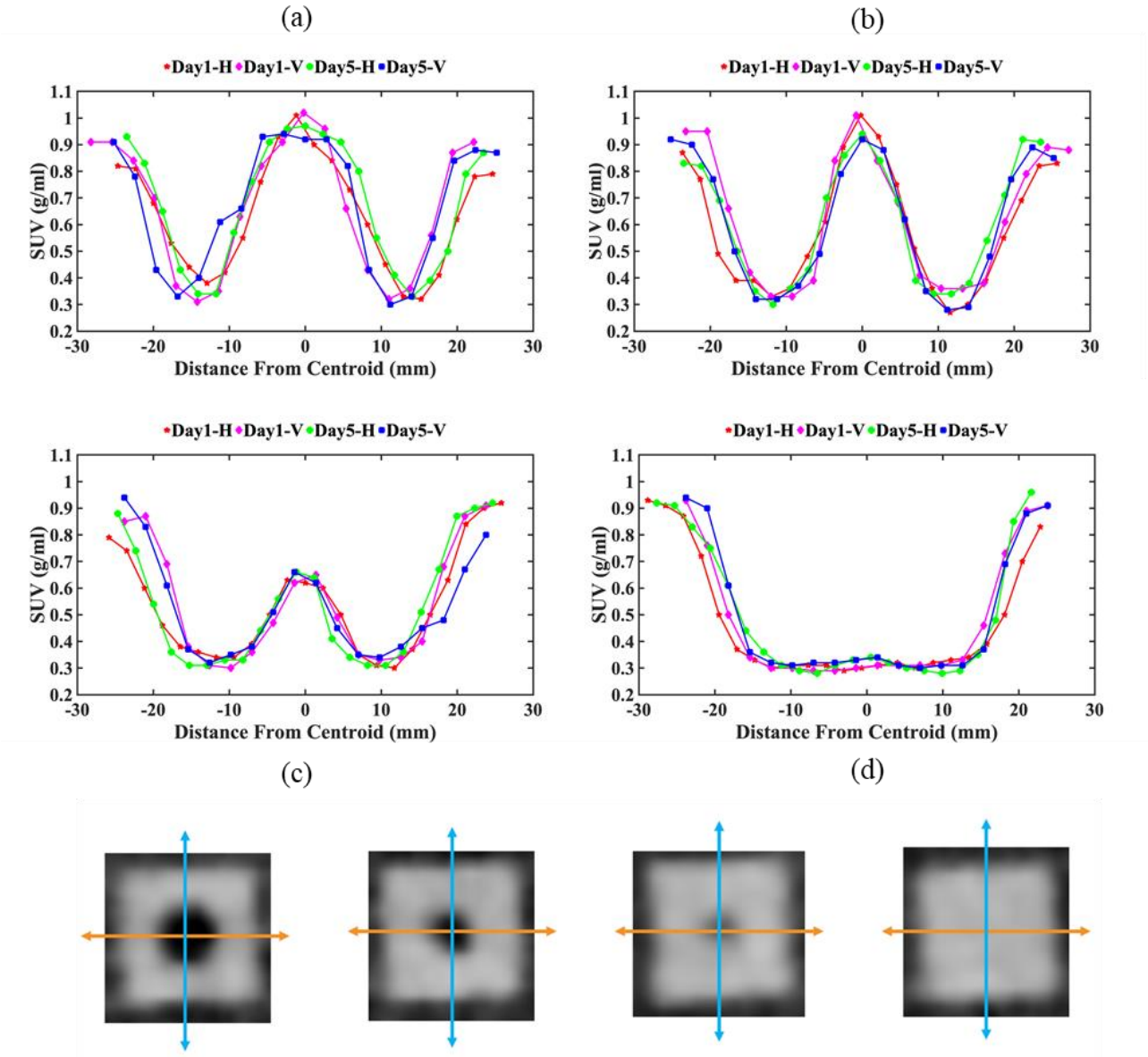

Figure A4. Day 1 vs Day 5 - SUV Profile along Vertical and Horizontal direction vectors from Cube centroid on Axial Plane : (a) 70-5-20, (b) 70-5-15, (c) 70-5-10, (d) 70-5-0; Reference for Profile Extraction on Cropped PET Image (Bottom) – Only Day – 1 and Day – 5 were selected based on highest pairwise Wilcox *p* values , effective activity during first scan and layer variability criteria

NOTE: This preprint reports new research that is not certified by peer review and should not be used to guide clinical practice.

References:

1. Ljungberg M. Instrumentation, Calibration, Quantitative Imaging, and Quality Control. In: Radiotheranostics - A Primer for Medical Physicists I. CRC Press; 2024.

2. McDougald WA, Mannheim JG. Understanding the importance of quality control and quality assurance in preclinical PET/CT imaging. EJNMMI Phys. 2022 Oct 31;9(1):77.

3. Reynés-Llompart G, Zorz A, Boellaard R, Ptáček J, Pike L, Soret M, et al. Quality control in PET/CT and PET/MRI: Results of a survey amongst European countries. Phys Med. 2022 Jul 1;99:16–21.

4. Internationale Atomenergie-Organisation. Quality assurance for PET and PET/CT systems. Vienna: Internat. Atomic Energy Agency; 2009. 145 p. (IAEA human health series).

5. Koole M, Armstrong I, Krizsan AK, Stromvall A, Visvikis D, Sattler B, et al. EANM guidelines for PET-CT and PET-MR routine quality control. Z Für Med Phys. 2023 Feb 1;33(1):103–13.

6. D'Arienzo M, Pimpinella M, Capogni M, De Coste V, Filippi L, Spezi E, et al. Phantom validation of quantitative Y-90 PET/CT-based dosimetry in liver radioembolization. EJNMMI Res. 2017 Dec;7(1):94.

7. Lu S, Zhang P, Li C, Sun J, Liu W, Zhang P. A NIM PET/CT phantom for evaluating the PET image quality of micro-lesions and the performance parameters of CT. BMC Med Imaging. 2021 Dec;21(1):165.

8. Kidera D, Kihara K, Akamatsu G, Mikasa S, Taniguchi T, Tsutsui Y, et al. The edge artifact in the point-spread function-based PET reconstruction at different sphere-to-background ratios of radioactivity. Ann Nucl Med. 2016 Feb 1;30(2):97–103.

9. Munk OL, Tolbod LP, Hansen SB, Bogsrud TV. Point-spread function reconstructed PET images of sub-centimeter lesions are not quantitative. EJNMMI Phys. 2017 Jan 13;4(1):5.

10. Berthon B, Marshall C, Edwards A, Evans M, Spezi E. Influence of cold walls on PET image quantification and volume segmentation: A phantom study. Med Phys. 2013;40(8):082505.

11. Tong S, Alessio A, Thielemans K, Stearns C, Ross S, Kinahan P. Edge artifacts in PSF-based PET image reconstruction: Characterization and mitigation. J Nucl Med. 2011 May 1;52(supplement 1):106–106.

12. Matheoud R, Boellaard R, Pike L, Ptacek J, Reynés-Llompart G, Soret M, et al. EFOMP's protocol quality controls in PET/CT and PET/MR. Phys Med. 2023 Jan;105:102506.

13. Maronnier Q, Courbon F, Caselles O. Evaluation of a method based on synthetic data inserted into raw data prior to reconstruction for the assessment of PET scanners. EJNMMI Phys. 2022 Oct 1;9(1):68.

14. Tandon P, Prakash D, Kheruka SC, Bhat NN. Quality Assurance in Positron Emission Tomography-Computed Tomography (PET-CT). In: Tandon P, Prakash D, Kheruka SC, Bhat NN, editors. Radiation Safety Guide for Nuclear Medicine Professionals [Internet]. Singapore: Springer Nature; 2022 [cited 2024 Nov 7]. p. 233–65. Available from: https://doi.org/10.1007/978-981-19-4518-2_17

15. Okamoto M, Takahashi K, Oda K, Satoh Y, Inaoka Y, Miyatake H, et al. Dedicated QC/QA phantom tools using traceable Ge-68/Ga-68 point-like sources for dbPET and PEM. J Nucl Med. 2019 May 1;60(supplement 1):2026–2026.

16. Chen MK, Menard DH, Cheng DW. Determining the Minimal Required Radioactivity of 18F-FDG for Reliable Semiquantification in PET/CT Imaging: A Phantom Study. J Nucl Med Technol. 2016 Mar;44(1):26–30.

NOTE: This preprint reports new research that is not certified by peer review and should not be used to guide clinical practice.

17. Fahey F, Christian P, Zukotynski K, Sexton-Stallone B, Kiss C, Clarke B, et al. Use of a Qualification Phantom for PET Brain Imaging in a Multicenter Consortium: A Collaboration Between the Pediatric Brain Tumor Consortium and the SNMMI Clinical Trials Network. J Nucl Med. 2019 May;60(5):677–82.

18. Sipilä O, Liukkonen J, Halme HL, Tolvanen T, Sohlberg A, Hakulinen M, et al. Variability in PET image quality and quantification measured with a permanently filled 68Ge-phantom: a multi-center study. EJNMMI Phys. 2023 Jun 16;10(1):38.

19. Gillett D, Marsden D, Ballout S, Attili B, Bird N, Heard S, et al. 3D printing 18F radioactive phantoms for PET imaging. EJNMMI Phys. 2021 Apr 28;8(1):38.

20. Mínguez Gabiña P, Monserrat Fuertes T, Jauregui I, del Amo C, Rodeño Ortiz de Zarate E, Gustafsson J. Activity recovery for differently shaped objects in quantitative SPECT. Phys Med Biol. 2023 Jun;68(12):125012.

21. Badea RA, Voicu AM, Orian A, Paraschiv B, Vasiliu A, David EC, et al. 3D PRINTED ANTHROPOMORPHIC DOSIMETRIC PHANTOMS RECONSTRUCTED FROM DICOM IMAGES. 2024.

22. Cavaliere C, Baldi D, Brancato V, Aiello M, Salvatore M. A customized anthropomorphic 3D-printed phantom to reproducibility assessment in computed tomography: an oncological case study. Front Oncol. 2023 Aug 28;13:1123796.

23. Cerviño L, Soultan D, Cornell M, Yock A, Pettersson N, Song WY, et al. A novel 3D-printed phantom insert for 4D PET/CT imaging and simultaneous integrated boost radiotherapy. Med Phys. 2017 Oct;44(10):5467–74.

24. Okkalidis N. 3D printing methods for radiological anthropomorphic phantoms. Phys Med Biol. 2022 Jul;67(15):15TR04.

25. Gear JI, Cummings C, Craig AJ, Divoli A, Long CDC, Tapner M, et al. Abdo-Man: a 3D-printed anthropomorphic phantom for validating quantitative SIRT. EJNMMI Phys. 2016 Dec;3(1):17.

26. Gear JI, Long C, Rushforth D, Chittenden SJ, Cummings C, Flux GD. Development of patient-specific molecular imaging phantoms using a 3D printer. Med Phys. 2014 Aug;41(8Part1):082502.

27. Gear JI, Cummings C, Sullivan J, Cooper-Rayner N, Downs P, Murray I, et al. Radioactive 3D printing for the production of molecular imaging phantoms. Phys Med Biol. 2020 Sep 7;65(17):175019.

28. Wollenweber SD, Alessio AM, Kinahan PE. A phantom design for assessment of detectability in PET imaging. Med Phys. 2016;43(9):5051–62.

29. Lam TO, Young A. Fabrication of 3D Printed Hollow Spheres for QC and Feasibility for Use With xSPECT Bone [Internet]. In Review; 2023 Jul [cited 2024 Jan 25]. Available from: https://www.researchsquare.com/article/rs-3126362/v1

30. Jessen L, Gustafsson J, Ljungberg M, Curkic-Kapidzic S, Imsirovic M, Sjögreen-Gleisner K. 3D printed non-uniform anthropomorphic phantoms for quantitative SPECT. EJNMMI Phys. 2024 Jan 22;11(1):8.

31. Hafiz HM, Noramaliza MN, Hasley RS, Fikri ASF. DEVELOPMENT AND DESIGN OF A 3D-PRINTED PHANTOM FOR PET-CT NUCLEAR IMAGING QUALITY CONTROL: THE FIRST PHASE OF THE STUDY. J Med Imaging Radiat Sci. 2023 Sep 1;54(3, Supplement):S18.

32. Wegner M, Krause D. 3D printed phantoms for medical imaging: recent developments and challenges. J Mech Sci Technol. 2024 Sep 1;38(9):4537–43.

NOTE: This preprint reports new research that is not certified by peer review and should not be used to guide clinical practice.

33. Läppchen T, Meier LP, Fürstner M, Prenosil GA, Krause T, Rominger A, et al. 3D printing of radioactive phantoms for nuclear medicine imaging. EJNMMI Phys. 2020 Apr 22;7(1):22.

34. Tang MZ, Choo HL, Yeong CH, Wong YH. Development of 3D-Printed Heterogeneous Tumour Phantom for Quantitative Analysis in PET/CT Imaging. MATEC Web Conf. 2021;335:03014.

35. Gallivanone F, Interlenghi M, D'Ambrosio D, Trifirò G, Castiglioni I. Parameters Influencing PET Imaging Features: A Phantom Study with Irregular and Heterogeneous Synthetic Lesions. Contrast Media Mol Imaging. 2018;2018(1):5324517.

36. Theisen AL, Lassmann M, Tran-Gia J. Toward a Patient-Specific Traceable Quantification of SPECT/CT-Based Radiopharmaceutical Distributions. J Nucl Med. 2022 Jul;63(7):1108.

37. Qiu J, Hou K, Dyer BA, Chen JC, Shi L, Sun Y, et al. Constructing Customized Multimodal Phantoms Through 3D Printing: A Preliminary Evaluation. Front Phys [Internet]. 2021 Apr 27 [cited 2024 Nov 4];9. Available from: https://www.frontiersin.org/journals/physics/articles/10.3389/fphy.2021.605630/full

38. Asbai-Ghoudan R, Ruiz de Galarreta S, Rodriguez-Florez N. Analytical model for the prediction of permeability of triply periodic minimal surfaces. J Mech Behav Biomed Mater. 2021 Dec;124:104804.

39. Cholifah U, Nafiunisa A, Aryanti N, Wardhani DH. The influence of cocamide DEA towards the characteristics of transparent soap. IOP Conf Ser Mater Sci Eng. 2021 Feb;1053(1):012016.

40. The new opportunities for high time resolution clinical TOF PET | Clinical and Translational Imaging [Internet]. [cited 2025 Mar 17]. Available from: https://link.springer.com/article/10.1007/s40336-019-00316-5

41. Yildirim N, Simsek M, Aldemir MN, Bilici M, Tekin SB. Relationship between 18-FDG-PET/CT and Clinicopathological Features and Pathological Responses in Patients with Locally Advanced Breast Cancers. Eurasian J Med. 2019 Jun;51(2):154–9.

42. Qi C, Wang S, Yu H, Zhang Y, Hu P, Tan H, et al. An artificial intelligence-driven image quality assessment system for whole-body [18F]FDG PET/CT. Eur J Nucl Med Mol Imaging. 2023 Apr 1;50(5):1318–28.

43. Graef J, Senger C, Wetz C, Baur ADJ, Kluge AK, Lukas M, et al. Shortened Tracer Uptake Time in GA-68-DOTATOC-PET of Meningiomas Does Not Impair Diagnostic Accuracy and PET Volume Definition. Diagnostics. 2020 Dec;10(12):1084.

44. Luna CBB, Filho EA dos S, Siqueira DD, Araújo EM, Nascimento EP do, de Mélo TJA. Influence of Small Amounts of ABS and ABS-MA on PA6 Properties: Evaluation of Torque Rheometry, Mechanical, Thermomechanical, Thermal, Morphological, and Water Absorption Kinetics Characteristics. Materials. 2022 Jan;15(7):2502.

45. Leite M, Varanda A, Ribeiro AR, Silva A, Vaz MF. Mechanical properties and water absorption of surface modified ABS 3D printed by fused deposition modelling. Rapid Prototyp J. 2018 Jan 2;24(1):195–203.

46. Yavuz G, Kovan B, Toklu T, Çermik TF, Öztürk C. Calculation of recovery coefficients for partial volume effect correction in PET/CT imaging using a customized anthropomorphic body phantom. Biomed Eng OnLine. 2025 Feb 15;24(1):20.

47. Aide N, Lasnon C, Veit-Haibach P, Sera T, Sattler B, Boellaard R. EANM/EARL harmonization strategies in PET quantification: from daily practice to multicentre oncological studies. Eur J Nucl Med Mol Imaging. 2017;44(Suppl 1):17–31.

NOTE: This preprint reports new research that is not certified by peer review and should not be used to guide clinical practice.